Mantle plume migration ?

Chuansong He[1]

[1]Institute of Geophysics, China Earthquake Administration, Beijing 100081, China

Abstract: The stagnation and dehydration of the Pacific Plate slab in the mantle transition zone are widely accepted to have resulted in Mesozoic and Cenozoic volcanic activities and the formation of the Songliao Basin in NE China. However, this notion has been challenged by recent seismic studies. Alternatively, a mantle plume may have generated large-scale volcanism and led to the formation of the Songliao Basin. In this study, a detailed analysis involving common conversion point (CCP) stacking of receiver functions was carried out. The results reveal a significantly deepened region of the 410 km discontinuity and an elevated region of the 660 km discontinuity in the centre of NE China (or the Songliao Basin). The combination of these results with those of a previous study suggests that an upwelling mantle plume was located under the centre of the Songliao Basin in the Mesozoic. Furthermore, the distinctive structure of the mantle transition zone (MTZ) beneath the southern part of the Songliao Basin identified in this study is correspond to mantle plume upwelling (a mushroom-shaped low-velocity anomaly), which may be related to the Changbaishan volcanic activities in the Cenozoic.

[1] email:hechuansong@aliyun.com

Key words: Upwelling mantle plume; 410 km discontinuity; 660 km discontinuity; CCP stacking of receiver function; Songliao Basin; NE China.

1. Introduction

NE China, which includes the Xingan Massif, Jiamusi Massif and Songliao Massif, is located on the eastern margin of the Eurasian continent, is part of the Central Asian Orogenic Belt and is bounded by the Siberian craton to the north and the North China Craton to the south (Fig. 1). This region experienced the final closure of the Palaeo-Asian Ocean and the westward subduction of the Palaeo-Pacific Plate from the late Palaeozoic to the early Mesozoic (Tang et al., 2018; Xiao et al., 2015; Ryu and Lee, 2017; Wang et al., 2019; Sun et al., 2018), as well as intense Mesozoic-Cenozoic volcanism and the establishment of the Songliao Basin.

Since the 1990s, the concept of a stagnant slab in the mantle transition zone (MTZ) (MTZ is bounded by the 410 and 660 km discontinuities) generated by the subducted Pacific Plate has been widely accepted, and dehydration of this stagnant slab may be related to extensive volcanism in the Mesozoic and Cenozoic (Zhao et al., 1994; Zhao et al., 2019; Maruyama et al., 2009; Chen and Faccenda, 2019). This process is proposed to have resulted in related metallogenesis, tectonic extension, rifting processes and formation of the Songliao Basin (Wu et al., 2003; Bao and Niu, 2017; Yang et al., 2017).

However, whether the volcanism, rifting processes and Songliao Basin formation can be attributed to a stagnant slab in the MTZ is a matter of debate.

Recently, a number of tomographic and receiver function studies have been carried out in NE China and nearby regions (Ai et al., 2003; Li and Yuan, 200; Lei and Zhao, 2005; Gao et al., 2010; Tang et al., 2014; He et al., 2014; He and Santosh, 2016; Liu et al., 2017; Zhang et al., 2019; Fan et al., 2020; Kim et al., 2016; Zhu et al., 2019; Lu et al., 2020; Sun et al., 2020). Among them, some tomographic studies failed to observe significant high-velocity anomalies (or a stagnant slab) in the MTZ (e.g., Tang et al., 2014; He and Santosh, 2016). Additionally, receiver function studies have defined the topographies of the upper mantle discontinuities associated with thermal upwelling (He et al., 2014; He, 2019). However, common conversion point (CCP) stacking of receiver functions in previous studies used a single 1-D or pseudo 3-D velocity model (He et al., 2014; He et al., 2019); moreover, it does not consider the effect of S-wave velocity and slowness (He et al., 2014; He et al., 2019). Therefore, previous studies cannot define the detailed topographies of the 410 and 660 km discontinuities, which are a key indicator of the temperature variation in the upper mantle and closely related to the thermal upwelling of the mantle (Foulger, 2012).

In this study, the detailed topographies of the 410 and 660 km discontinuities were inferred from the CCP stacking of receiver functions. A 3-D global velocity model (Lu et al., 2019) and a local velocity model (He and Santosh, 2016) are used to correct the apparent

65 depths of the 410 and 660 km discontinuities. The results indicate that there are
66 significant variations in the 410 and 660 km discontinuities beneath the centre of NE
67 China (specifically, the Songliao Basin) and its southern part, which may be related to
68 mantle plume upwelling.
69
70 **2. Method and data**
71
72 In the study region, a total of 1220 teleseismic events were extracted from 127
73 permanent seismic stations recorded from 2007 to 2014, and 282 teleseismic events were
74 collected from 148 temporary seismic stations (Fig. 1). The events were limited to Ms >6.0,
75 and the earthquake epicentral distances ranged from 30° to 90° for individual
76 event-station pairs. A Butterworth bandpass filter between 0.05 and 1 Hz was applied to
77 the raw record, which was cut from 15 *s* before to 120 *s* after the P-wave arrival. To obtain
78 a high signal-to-noise ratio for all events, the waveform cross-correlation technique
79 (VanDecar and Crosson, 1990) was used to select consistent raw data (for example,
80 please see Fig. S1). In total, 21627 high-quality receiver functions were calculated by a
81 modified frequency-domain deconvolution with a 1 *Hz* Gaussian filter and 0.01 water level
82 (Langston, 1979; Zhu and Kannamori, 2000) (for example, please see Fig. S2).
83
84 The topographies of the 410 and 660 km discontinuities in the study region are defined
85 by the CCP technique (VanDecar and Crosson, 1997; Eagar et al., 2010; Zhu, 2000). The
86 spherical coordinates used to calculate Ps–P differential time T_{Ps} (Eagar et al., 2010):

$$T_{Ps} = \sum_i^N \left(\sqrt{\left(\frac{R_i}{V_{Si}}\right) - p_{Ps}^2} - \sqrt{\left(\frac{R_i}{V_{Pi}}\right) - p_P^2} \right) \frac{\Delta r}{R_i} \quad (1)$$

where p_{Ps} and p_P are the ray parameters of the direct Ps and P phases, respectively and V_{Pi} and V_{Si} are the P- and S-wave velocities, respectively, in the *i*th layer. R_i and Δr are the Earth's semidiameter at each *i*th depth shell (r_i) and depth interval, respectively. To ensure the reliability of the results, a 3-D global P- and S-wave velocity model by Lu et al. (2019) and local 3-D velocity model in the area by He and Santosh (2016) are employed to remove the velocity heterogeneity effects in the upper mantle. The Ps-P differential times in the 3-D model were presented as follows:

$$T_{Ps3D} = T_{Ps} + \Delta T \quad (2)$$

where ΔT is related to the 3-D velocity velocity perturbations or the travel time correction

A depth interval of 1 km and a lateral grid interval of 0.5° were designed in the grid of CCP stacking of receiver functions, and a radius (or bin) of 75 km used to search for the migrated receiver functions (Xu et al., 2018). In each bin, a total of 2000 resampling iterations of the bootstrap resampling are employed to calculate the standard deviation and mean value.

3. Results

In Fig. 2, there are no obvious changes in the 410 and 660 km discontinuities in profiles a and b (Fig. 2 a, b). In contrast, at the centres of profiles c and d, the 410 km discontinuity shows significant deepening by approximately 15 km (Fig. 2c, d; blue rectangle), whereas the 660 km discontinuity exhibits significant shallowing by approximately 20 km (Fig. 2 c). Previous receiver function studies show results similar to those of the c profile (He, 2019); however, the 410 and 660 km discontinuities of the d profile did not have any signature of the anomaly (He, 2019). The 660 km discontinuity appears topographically elevated in the centres of profiles e and f (Fig. 2 e, f; yellow rectangle).

To further clarify the relationship between the upwelling mantle plume and the upper mantle discontinuities, the P-wave velocity perturbation profiles (He and Santosh, 2016) (e and f profiles of Fig. S4) are overlain on the CCP stacking profiles of the receiver functions (e and f profiles of Fig. 2) (Fig. 3). The results indicate that the elevated location of the 660 km discontinuity correspond well to that of an upwelling mantle plume (Fig. 3e, f; white rectangle region).

Additionally, 6 CCP stacking profiles (g-l) of receiver functions were created (Fig. 4; for the locations of the profiles, please see Fig. 1). The images from the CCP stacking of receiver functions show a deepened region for the 410 km discontinuity and an elevated

region for the 660 km discontinuity at the centres of the profiles (Songliao Basin) (Fig. 4 i, j, regions indicated by the blue rectangles). An elevated region for the 660 km discontinuity at the centres of the k and l profiles, which corresponds to the location of the upwelling mantle plume (Fig. 4 k, l, regions indicated by the yellow rectangles).

The depths of the 410 and 660 km discontinuities and the MTZ thickness in the study region have been extracted (Fig. 5 e, f and g). The results show a deepened region for the 410 km discontinuity (Fig. 5e, white circle region) and an elevated region for the 660 km discontinuity (Fig. 5 f, white circle region), resulting in thinning of the MTZ thickness (Fig. 5 g, white circle region) in the centre of NE China (specifically, the Songliao Basin). At southern part of the Songliao Basin, the 410 km discontinuity appears to be relatively deep, with slight shallowing in a localized region (Fig. 5e, green circle region); the 660 km discontinuity appears to be relatively shallow (Fig. 5f, green circle region); and the MTZ is therefore relatively thin (Fig. 5g, green circle region).

Meanwhile, a local 3-D velocity model (He and Santosh, 2016) was used to correct the CCP stacking results of the receiver function, and the S-wave velocity was calculated from the Vp/Vs ratio of the AK135 velocity model (Kennett et al., 1995). The results indicate that the topographies of the 410 and 660 km discontinuities and the MTZ thickness beneath the centre of NE China and its southern part inferred from this model are basically consistent with those from the 3-D global P- and S-wave velocity model (Lu et al., 2019).

4. Discussion

4.1 Mesozoic mantle plume and migration of the mantle plume

Receiver functions are the most popular tool for investigating the 410 and 660 km discontinuities and the structure of the MTZ (Agius et al., 2017). Imaging the topographies of the 410 and 660 km discontinuities and the MTZ thickness plays a key role in understanding the thermal conditions of the MTZ (He et al., 2014; Zhang et al., 2019), thereby providing an indication of mantle convection within the Earth (Foulger, 2012).

Based on seismic imaging and mineral physical experiments (Katsura and Ito,1989; Ito and Takahashi, 1989; Ringwood, 1975; Deuss, 2006), the 410 discontinuity, which exhibits a positive Clapeyron slope, involves the phase transition of olivine to wadsleyite (Helffrich, 2000; Kawai et al., 2013; Jenkins et al., 2016; Frost, 2008), and the temperature increases with increasing depth. In contrast, the 660 discontinuity, which exhibits a negative Clapeyron slope, is likely associated with the phase transition of ringwoodite to perovskite and magnesiowüsite (Helffrich, 2000; Kawai et al., 2013; Jenkins et al., 2016), and the temperature increases with decreasing depth.

Mantle plumes are expected to affect the topographies of the 410 and 660 km discontinuities and the MTZ thickness because they pass through the MTZ and have

175 higher temperatures than the surrounding mantle (Deuss, 2007). Consequently, mantle
176 plumes might deepen the topography of the 410 km discontinuity (deepening 15-20 km)
177 and elevate the topography of the 660 km discontinuity, resulting in MTZ thinning (Shen et
178 al., 2002). Thus, the results identified in this study show that the features of the 410 and
179 660 km discontinuities and the MTZ in the centre of NE China (specifically, the Songliao
180 Basin) may be related to mantle plume upwelling (Fig. 5, Fig. 6).
181
182 Upwelling mantle plumes can generate lower crustal underplating (Pirajno, 2007),
183 which led to high Vp/Vs ratio in the crust (or lower crust). A previous receiver function (He
184 et al., 2016) study concluded that high Vp/Vs ratios (possibly related to lower crustal
185 magmatic underplating induced by upwelling mantle plume) and crustal thinning exists in
186 the centre of NE China (the Songliao Basin) (Fig. 7a, b). The large areas of continental rift
187 basalt that formed in NE China during the Late Jurassic to Late Cretaceous are
188 associated with an upwelling mantle plume (Ren et al., 2002). Geological studies have
189 also found that basalts erupted from more than 590 volcanoes across an area of
190 approximately 50,000 km^2 in the Songliao Basin in the Mesozoic (Liu et al., 2001), which
191 may be related to upwelling mantle plume; in contrast, volcanism was relatively rare on
192 the margins of the Songliao Basin in the Mesozoic (Liu et al., 2001). These results support
193 the interpretation that the MTZ structure beneath NE China (specifically, the Songliao
194 Basin) may be a relic of Mesozoic mantle plume upwelling, which might be related to the
195 formation of the Songliao Basin (He et al., 2014).
196

However, tomographic data do not reveal a relic of mantle plume upwelling beneath the Songliao Basin; in contrast, tomographic data define a relic of mantle plume upwelling under the southern margin of the Songliao Basin (Fig. S4 e, f) (Tang et al., 2014; He and Santosh, 2016). Relics of upwelling mantle plumes can be retained for several million to several billion years (Burk and Torsvik, 2004; Chang and Van der Lee, 2011). Thus, the relic of the upwelling Mesozoic mantle plume should not have disappeared. Therefore, it is proposed that the upwelling mantle plume beneath the Songliao Basin may have migrated to the current position defined by tomography (He and Santosh, 2016) (Fig. 8). Based on the results identified in the tomography (He and Santosh, 2016) (Fig. 3), it is suggested that the upwelling mantle plume might occur title from west to east during the migration process.

Volcanism showed a spatial shift from the centre of the Songliao Basin to the edges of the basin, and the products of this volcanism decrease in age from west to the east in NE China (Sun et al., 2020), which may be related to the migration and tilte of the upwelling mantle plume. Recent seismic studies have reported that the plume beneath Hawaii has also migrated rather than remaining stationary (Torsvik et al., 2017).

4.2. Cenozoic mantle plume

Since approximately 2.77 Ma, the CBS, located on the eastern margin of the Songliao Basin, has produced a series of eruptions (Wang et al., 2003) that have affected an area

with a diameter of 300 km (Kuritani et al., 1982). The distinctive structure of the MTZ (Fig. 2 e, f, Fig. 5 and Fig. 6) identified in this study might be indicative of an upwelling mantle plume at the southern part of the Songliao Basin (Fig. 8); moreover, the surface projection of the upwelling mantle plume identified by tomography (He and Santosh, 2016) corresponds to the CBS (Fig. 1; Fig. S4, profile e and f). Therefore, mantle plume upwelling may have contributed to the Cenozoic volcanism of the CBS (Turcotte and Schubert, 1982). Rare earth element (REE) studies indicate that the magmatism of the CBS is related to a mantle source and might be associated with mantle plume upwelling in the Cenozoic (Fan et al., 2007; Basu et al., 1991).

5. Conclusions

The results identified in this study indicate that a relic of an upwelling mantle plume exists beneath the Songliao Basin, which may be related to large-scale volcanism and Songliao Basin formation in the Mesozoic. There is a possibility that the Mesozoic plume may have migrated to the southern part of the Songliao Basin and occured title.

A deepened region of the 410 km discontinuity and an elevated region of the 660 km discontinuity as well as the thinning of the MTZ in the southern part of the Songliao Basin identified in this study correspond to the mushroom-shaped low-velocity anomaly (or upwelling mantle plume) identified in the previous topographies. Its surface project correspond to the CBS, which implied that mantle plume upwelling might result in the

241 formation of the Changbaishan volcanism in the Cenozoic.

242

243 **Acknowledgements**

244

245 Thanks to the National Key RandD Plan of China (2017YFC601406), the Data
246 Management Centre of the China National Seismic Network at the Institute of Geophysics
247 and the China Earthquake Networks Centre. The data involved in the CCP stacking of
248 receiver functions can be accessed via https://doi.org/10.5281/zenodo.3762789.

249

250 **References**

251

252 Agius, M.R., Rychert, C.A., Harmon, N. and Laske, G. .2017. Mapping the mantle
253 transition zone beneath Hawaii from Ps receiver functions: Evidence for a hot plume
254 and cold mantle downwellings. *Earth Planet. Sci. Lett.,* **474**, 226-236.
255 Ai, Y.S., Zheng, T.Y., Xu, W.W., He, Y.M. and Dong, D.A .2003. A complex 660 km
256 discontinuity beneath northeast China. *Earth Planet. Sci. Lett.,* **212**, 63-71.
257 Bao, Y. and Niu, F. 2017. Constraining sedimentary structure using frequency dependent
258 P wave particle motion: A case study of the Songliao Basin in NE China. *J. Geophys.*
259 *Res.,* **122**, 9083-9094.
260 Basu, A.R., Wang, J.W., Huang, W.K., Xie, G.H. and Tatsumoto, M. 1991. Major element,
261 REE, and Pb, Nd and Sr isotopic geochemistry of Cenozoic volcanic rocks of eastern
262 China: implications for their origin from suboceanic-type mantle reservoirs. *Earth*

263 *Planet. Sci. Lett.,* **105**, 149-169.

264 Burke, K. and Torsvik, T.H. 2004. Derivation of Large Igneous Provinces of the past 200
265 million years from long-term heterogeneities in the deep mantle. *Earth Planet. Sci.*
266 *Lett.,* **227**, 531-538.

267 Chang, S.J. and Van der Lee, S. 2011. Mantle plumes and associated flow beneath
268 Arabia and East Africa. *Earth Planet. Sci. Lett.,* **302**, 448-454.

269 Chen, L. and Faccenda, M. 2019. Subduction‐induced upwelling of a hydrous transition
270 zone: Implications for the Cenozoic magmatism in northeast China. *J. Geophys. Res.,*
271 **124**, 11,489-11,504.

272 Deuss, A. 2007. Seismic observations of transition-zone discontinuities beneath hotspot
273 locations. *Geol. Soc. Am. Spec. Pap.,* **430**, 121-136.

274 Deuss, A., Redfern, S.A.T., Chambers, K. and Woodhouse, J. H. 2006. The nature of the
275 660‐kilometer discontinuity in Earth's mantle from global seismic observations of PP
276 precursors. *Science,* **311**, 198-201.

277 Dueker, K.G. and Sheehan, A.F. 1997. Mantle discontinuity structure from midpoint stacks
278 of converted P to S waves across the Yellowstone hotspot track. *J. Geophys. Res.,*
279 **102**, 8313-8327.

280 Eagar, K.C., Fouch, M.J. and James, D.E. 2010. Receiver function imaging of upper
281 mantle complexity beneath the Pacific Northwest, United States. *Earth Planet. Sci.*
282 *Lett.,* **297**, 141-153.

283 Efron, B. and Tibshirani, R.B.1986. Bootstrap methods for standard errors, confidence
284 intervals, and other measures of statistical accuracy. *Stat. Sci*., **1**, 54-75.

285 Fan, Q.C., Sui, J.l., Wang, T.H., Li, N. and Sun, Q. 2007. History of Volcanic Activity,
286 Magma Evolution and Eruptive Mechanisms of the Changbai Volcanic Province. *Geol.*
287 *J. China Univ.,* **13,** 175-190 (in Chinese with English abstract).
288 Fan, X., Chen, Q.F., Legendre, C.P. and Guo, Z. 2020. Intraplate volcanism
289 and regional geodynamics in NE Asia revealed by anisotropic Rayleigh‐
290 wave tomography. *Geophys. Res. Lett.,* **47**, e2019GL085623.
291 Frost, D. J. 2008. The upper mantle and transition zone. *Elements* 4, 171-176.
292 Foulger, G.R. 2012. Are 'hot spots' hot spots?. *J. Geodyn.*, *58*, 1-28.
293 Gao, Y., Suetsugu, D., Fukaob, Y., Obayashib, M., Shi, Y.T., Liu, R.F. 2010. Seismic
294 discontinuities in the mantle transition zone and at the top of the lower mantle
295 beneath eastern China and Korea: Influence of the stagnant Pacific slab. *Phys. Earth*
296 *Planet. Inter.,* **183**, 288-295.
297 He, C.S. 2019. Evidence for an upwelling mantle plume beneath the Songliao Basin,
298 Northeast China. *Phys. Earth Planet. Inter.,* **297**, 106316.
299 He, C.S., Dong, S.W., Chen, X.H., Santosh, M. and Niu, S.Y. 2014. Seisic evidence for
300 plume-induced rifting in the Songliao basin of Northeast China. *Tectonophysics* **627**,
301 171-181.
302 He, C.S. and Santosh, M. 2016. Seismic tomographic evidence for upwelling mantle
303 plume in NE China. Phys. *Earth Planet. Inter.,* **254**, 37-45.
304 Helffrich, G. 2000. Topography of the transition zone seismic discontinuities. *Rev.*
305 *Geophy.,* **38**, 141-158.
306 Ito, E. and Takahashi, E. 1989. Postspinel transformations in the system

307 Mg2SiO4-Fe2Si04 and some geophysical implications. *J. Geophys. Res.,* **94**,
308 10637-10646.
309 Jenkins, J., Cottaar, S., White, R.S. and Deuss. A. 2016.
310 Depressed mantle discontinuities beneath Iceland: Evidence of a garnet controlled 6
311 60 km discontinuity?. *Earth Planet. Sci. Lett.,* **433**, 159-168.
312 Katsura, T. and Ito, E. 1989. The system Mg2SiO4-Fe2SiO4 at high pressures and
313 temperatures: Precise determination of stabilities of olivine, modified spinel, and
314 spinel. *J. Geophys. Res.,* **94**, 15663-15670.
315 Kawai, K., Yamamoto, S., Tsuchiya, T. and Maruyama, S. 2013. The second continent:
316 Existence of granitic continental materials around the bottom of the mantle transition
317 zone. *Geosci. Front.,* **4**, 1-6.
318 Kennett, B.L.N., Engdahl, E.R. and Buland, R. 1995. Constraints on seismic velocities in
319 the Earth from traveltimes. *Geophys. J. Int.,* **122**, 108-124.
320 Kim, S., Tkalčić, H., Rhie, J. and Chen, Y. 2016. Intraplate volcanism controlled by
321 back-arc and continental structures in NE Asia inferred from transdimensional
322 Bayesian ambient noise tomography. *Geophys. Res. Lett.,* **43**, 8390-8398.
323 Kuritani, T., Ohtani, E. and Kimura, J.I. 2011. Intensive hydration of themantle transition
324 zone beneath China caused by ancient slab stagnation. *Nat. Geosci.,* **4**, 713-716.
325 Maruyama, S., Hasegawa, A., Santosh, M., Kogiso, T., Omori, S., Nakamura, H., Kawai,
326 K., Zhao, D. 2009. The dynamics of big mantle wedge, magma factory, and
327 metamorphic-metasomatic factory in subduction zones. *Gondwana Res.,* **16**,
328 414-430.

329 Langston, C.A. 1979. Structure under Mount Rainier, Washington, inferred from
330 teleseismic body waves. *J. Geophys. Res.,* **84**, 4749-4762.
331 Lei, J.S. and Zhao, D. 2005. P-wave tomography and origin of the Changbai intraplate
332 volcano in Northeast Asia. *Tectonophysics,* **397**, 281-295.
333 Li, X.Q. and Yuan, X.H. 2003. Receiver functions in northeast China - implications for slab
334 penetration into the lower mantle in northwest Pacific subduction zone. *Earth Planet.*
335 *Sci. Lett.,* **216**, 679-691.
336 Liu, J., Han, J. and Fyfe, W.S. 2001. Cenozoic episodic volcanism and continental rift-ing
337 in northeast China and possible link to Japan Sea development as revealed from K–Ar
338 geochronology. *Tectonophysics,* **339**, 385-401.
339 Liu, Y.N., Niu, F.L., Chen, M. and Yang, W.C. 2017. 3-D crustal and uppermost mantle
340 structure beneath NE China revealed by ambient noise adjoint tomography. *Earth*
341 *Planet. Sci. Lett.,* **461**, 20-29.
342 Lu, C., Grand, S.P., Lai, H. and Garnero, E.J. 2019. TX2019slab: A New P and S
343 Tomography Model Incorporating Subducting Slabs. *J. Geophys. Res*., **124**,
344 11549-11567.
345 Lu, M., Lei, J., Zhao, D., Ai, Y., Xu, X. and Zhang, G. 2020. SKS splitting measurements in
346 NE China: New insights into the Wudalianchi intraplate volcanism and mantle dynamics.
347 *J. Geophys. Res.,* **125**, e2019JB018575.
348 Pilidou, S., Priestley, K., Debayle, E. and Gudmundsson, Ó. 2005. Rayleigh wave
349 tomography in the North Atlantic: high resolution images of the Iceland, Azores and
350 Eifel mantle plumes. *Lithos, 79,* 453-474.

Phillips, E.H., Sims, K. W.W., Blichert-Toft, J., Aster, R.C., Gaetani, G.A., Kyle, P.R., Wallace, P.J. and Rasmussen, D.J. 2018. The nature and evolution of mantle upwelling at Ross Island, Antarctica, with implications for the source of HIMU lavas. *Earth Planet. Sci. Lett., 498*, 38-53.

Pirajno, F. 2007. Ancient to modern earth: the role of mantle plume in the making of continental crust: Earth's Oldest Rocks, edited by Kranendonk, M.J.V., Smithies, R.H., and Bennett, V.C., Developments in Precambrian Geology, v.15 (K.C. Condie, Series Editor).

Ren, J.Y., Tamaki, K., Li, S.T. and Zhang, J.X. 2002. Late Mesozoic and Cenozoic rifting and its dynamic setting in Eastern China and adjacent areas. *Tectonophysics,* **344**, 175-205.

Ringwood, A. 1975. Composition and Petrology of the Earth's Mantle. McGraw-Hill, New York, 618.

Ryu, I.C. and Lee, C. 2017. Intracontinental mantle plume and its implications for the Cretaceous tectonic history. *Earth Planet. Sci. Lett.,* **479**, 206-218.

Shaw, A.M., Hauri, E.H., Behn, M.D., Hilton, D.R., Macpherson, C.G. and Sinton, J.M. 2012. Long-term preservation of slab signatures in the mantle inferred from hydrogen isotopes. *Nat. Geosci.,* **5**, 224-228.

Shen, Y., Solomon, S.C., . Bjarnason, I.T., Nolet, G., Morgan, W.J., Allen, R.M. Kristin, V., Jakobsdóttir, S., Stefánsson, R., Julian, B.R., Foulger, G.R. 2002. Seismic evidence for a tilted mantle plume and north-south mantle flow beneath Iceland. *Earth Planet. Sci. Lett.,* **197**, 261-272.

373 Sun, M., Chen, H., Milan, L. A., Wilde, S. A., Jourdan, F. and Xu, Y. 2018. Continental arc
374 and back-arc migration in eastern NE China: New constraints on Cretaceous
375 Paleo-Pacific subduction and rollback. *Tectonics*, **37**, 3893-3915.
376 Sun, M., Gao, S.S., Liu, K.H. and Fu, X.F. 2020. Upper mantle and mantle transition zone
377 thermal and water content anomalies beneath NE Asia: Constraints from receiver
378 function imaging of the 410 and 660km discontinuities. *Earth Planet. Sci. Lett.,* **532**,
379 116040.
380 Tang, J., Xu, W.L., Wang, F. and Ge, W.C. 2018. Subduction history of the Paleo‐Pacific
381 slab beneath Eurasian continent: Mesozoic‐Paleogene magmatic records in
382 Northeast Asia. *Sci. China-D,* **61**, 527-559.
383 Tang, Y., Obayashi, M., Niu, F., Grand, S.P., Chen, Y.J., Kawakatsu, H., Tanaka, S., Ning,
384 J. and Ni, J.F. 2014. Changbaishan volcanism in NE China linked to
385 subduction-induced mantle upwelling. *Nat. Geosci*., **7**, 470.
386 Torsvik, T., Doubrovine, P., Steinberger, B. Gaina, C., Spakman, W. and Domeier, M.
387 2017. Pacific plate motion change caused the Hawaiian-Emperor Bend. *Nat.*
388 *Commun.,* **8**, 15660.
389 Turcotte, D. and Schubert, G. 1982. Geodynamics Applications of Continuum Physics to
390 Geological Problems. John Wiley, New York, pp.1-449.
391 Tang, H.F., Kong, T., Wu, C.Z., Wang, P.J., Peng, X., Gao, Y.F., 2017. Filling Pattern of
392 Volcanostratigraphy of Cenozoic Volcanic Rocks in the Changbaishan Area and
393 Possible Future Eruptions. *Acta Geologica Sinica,* **91**, 1717-1732.
394 VanDecar, J.C. and Crosson, R.S. 1990. Determination of teleseismic relative phase

arrival times using multi-channel cross-correlation and least squares. *Bull. Seismol. Soc. Am.,* **80**, 150-169.

Wang, F., Xu, W.L., Xing, K.C., Wang, Y.N., Zhang, H.H., Wu, W., Sun, C.Y. and Ge, W.C. 2019. Final closure of the Paleo‐Asian Ocean and onset of subduction of Paleo-Pacific Ocean: constraints from early Mesozoic magmatism in central southern Jilin Province, NE China. *J. Geophys. Res.,* **124**, 2601-2622.

Wang, Y., Li, C., Wei, H. and Shan, X. 2003. Late Pliocene–recent tectonic setting for the Tianchi volcanic zone, Changbai Mountains, northeast China. J*. Asian Earth Sci.,* **21**, 1159-1170.

Wu, F.Y., Ge, W.C., Sun, D.Y. and Guo, C.L. 2003. Discussions on the lithospheric thinning in eastern China. *Earth Sci. Front.,* **10**, 51-60 (in Chinese with English abstract).

Xiao W.J., Windley, B.F., Sun, S., Li, J.L., Huang, B.C., Han, C.M., Yuan, C., Sun, M. and Chen, H.L. 2015. A tale of amalgamation of three Permo-Triassic collage systems in Central Asia: Oroclines, sutures, and terminal accretion. *Annu. Rev. Eearth Pl. Sc.,* **43**, 477-507.

Xu, M.J., Huang, H., Huang, Z.C., Wang, P., Wang, L.S., Xu, M.J., Mi, N., Li, H., Yu, D.Y. and Yuan, X.H. 2018. Insight into the subducted Indian slab and origin of the Tengchong volcano in SE Tibet from receiver function analysis. *Earth Planet. Sci. Lett.,* **482**, 567-579.

Yang, T., Moresi, L., Zhao, D., Sandiford, D. and Whittaker, J. 2018. Cenozoic lithospheric deformation in Northeast Asia and the rapidly-aging Pacific Plate. *Earth Planet. Sci.*

Lett., **492**, 1-11.

Zhang, M., Sun, D., Wang, Y. and Wu, Z. 2019. Fine structure of the 660‐km discontinuity beneath southeastern China. *Geophys. Res. Lett.,* **46**, 7304-7314.

Zhao, D., Hasegawa, A. and Kanamori, H. 1994. Deep structure of Japan subduction zones as derived from local,regional, and teleseismic events. *J. Geophys. Res.,* **99**, 22313-22329.

Zhao, Y., Zhang, Y., Geng, M., Jiang, J. and Zou, X. 2019. Involvement of slab‐derived fluid in the generation of Cenozoic basalts in Northeast China inferred from machine learning. *Geophys. Res. Lett.,* **46**, 5234-5242.

Zhu, H., Tian, Y., Zhao, D., Li, H. and Liu, C. 2019. Seismic structure of the Changbai intraplate volcano in NE China from joint inversion of ambient noise and receiver functions. *J. Geophys. Res.,* **124**, 4984-5002.

Zhu, L. 2000. Crustal structure across the San Andreas Fault, southern California from teleseismic converted waves. *Earth Planet. Sci. Lett.,* **179**, 183-190.

Zhu, L. and Kanamori, H. 2000. Moho depth variation in southern California from teleseismic receiver functions. *J. Geophys. Res.,* **105**, 2069-2980.

Figure's captions:

Fig. 1. Left panel: location of the study region. Inset: distribution of events used in this study; blue dots: events collected from permanent seismic stations; red dots: events collected from the YP temporary seismic network; green dots: events collected from the XI

temporary seismic network. Right panel: Tectonic framework of NE China. Black triangles: permanent seismic stations, blue triangles: YP temporary seismic network, green triangles: XI temporary seismic network; a-f: profiles of P-wave velocity perturbation and CCP stacking of receiver functions (the locations are the same as those in a previous receiver function study (He, 2019); g-l: CCP stacking profiles of receiver functions. WDL: Wudalianchi volcano region, CBS: Changbaishan volcano zone. White lines: tectonic boundaries.

Fig. 2. CCP stacking profiles of the receiver functions (a-f). Blue rectangle: deepened region of the 410 km discontinuity and elevated region of the 660 km discontinuity at the centres of profiles c and d. The dataset was resampled and calculated with stacked amplitudes 2000 times by employing the bootstrapping method, and the final mean receiver functions corresponding to the 95% confidence level were calculated (Fig. S3). 410 km and 660 km are the upper mantle discontinuities, respectively.

Fig. 3. P-wave perturbation profiles overlain on CCP stacking profiles of receiver functions (profiles e and f of Fig. 2; for the locations of the profiles, please see Fig. 1).

Fig. 4. CCP stacking profiles (g-l). The dataset was resampled and calculated with stacked amplitudes 2000 times by employing the bootstrapping method, and the final mean receiver functions corresponding to the 95% confidence level were calculated (Fig. S5). 410 km and 660 km are the upper mantle discontinuities.

Fig. 5. Piercing points at depth of the 410 km (a) and depth of the 660 km (b), as calculated by the 1-D AK135 velocity model (Kennett et al., 1995). The piercing points are reasonably distributed at depths of 410 and 660 km (a and b). The numbers of stacking amplitudes at the 410 km discontinuity (c) and 660 km discontinuity (d), which are greater than 100. Depths of the 410 km discontinuity (e) and 660 km discontinuity (f) and the MTZ thickness (g). Depths of the 410 and 660 km discontinuities and the MTZ thickness after correction on the basis of a 3-D global P- and S-wave velocity model (Lu et al., 2019) and removal of the effects of velocity heterogeneities in the upper mantle. The dataset was resampled and calculated with stacked amplitudes 2000 times by employing the bootstrapping method, and the final mean receiver functions corresponding to the 95% confidence level were calculated. WDL: Wudalianchi volcano region; CBS: Changbaishan volcano zone.

Fig. 6. Depths of the 410 km discontinuity (a) and 660 km discontinuity (b) and the MTZ thickness (c), which have been corrected on the basis of a local 3-D velocity model (He and Santosh, 2016) and have had the effects of velocity heterogeneities in the upper mantle removed. The number of stacking amplitude points is greater than 100. The dataset was resampled and calculated with stacked amplitudes 2000 times by employing the bootstrapping method, and the final mean receiver functions corresponding to the 95% confidence level were calculated. WDL: Wudalianchi volcano region; CBS: Changbaishan volcano zone.

Fig. 7. Distribution of the crustal thickness (a) and Vp/Vs ratio (b) (He and Santosh, 2016).

Fig. 8 Model defined in this study. Hollow arrow: migration direction of the upwelling mantle plume. Dashed line: original location of the upwelling mantle plume in the Mesozoic.

Author contributions

H.C. conducted the analysis, interpreted the results and wrote the manuscript.

Additional information

Competing Interests: The author declares no competing interests.

Electronic supplementary material

Supplementary Information

Figure 1.

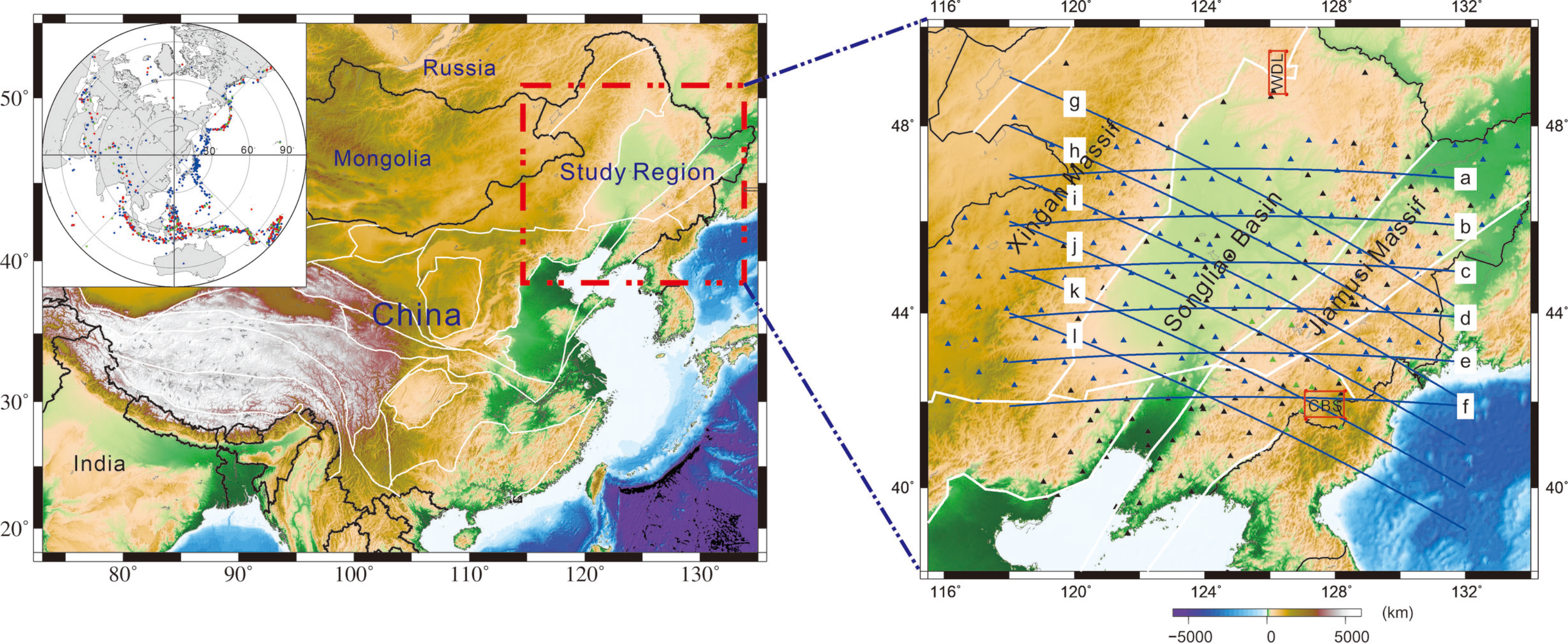
Russia
Mongolia
Study Region
China
India
80°
60°
90°
50°
40°
30°
20°
80°
90°
100°
110°
120°
130°
116°
120°
124°
128°
132°
48°
44°
40°
WDL
CBS
g
h
i
j
k
l
a
b
c
d
e
f
Xingan Massif
Songliao Basin
Jiamusi Massif
(km)
−5000
0
5000

Figure 2.

a
b
c
d
e
f
410 km
660 km
Depth (km)
300
400
500
600
700
800
−600
−400
−200
0
200
400
600

Figure 3.

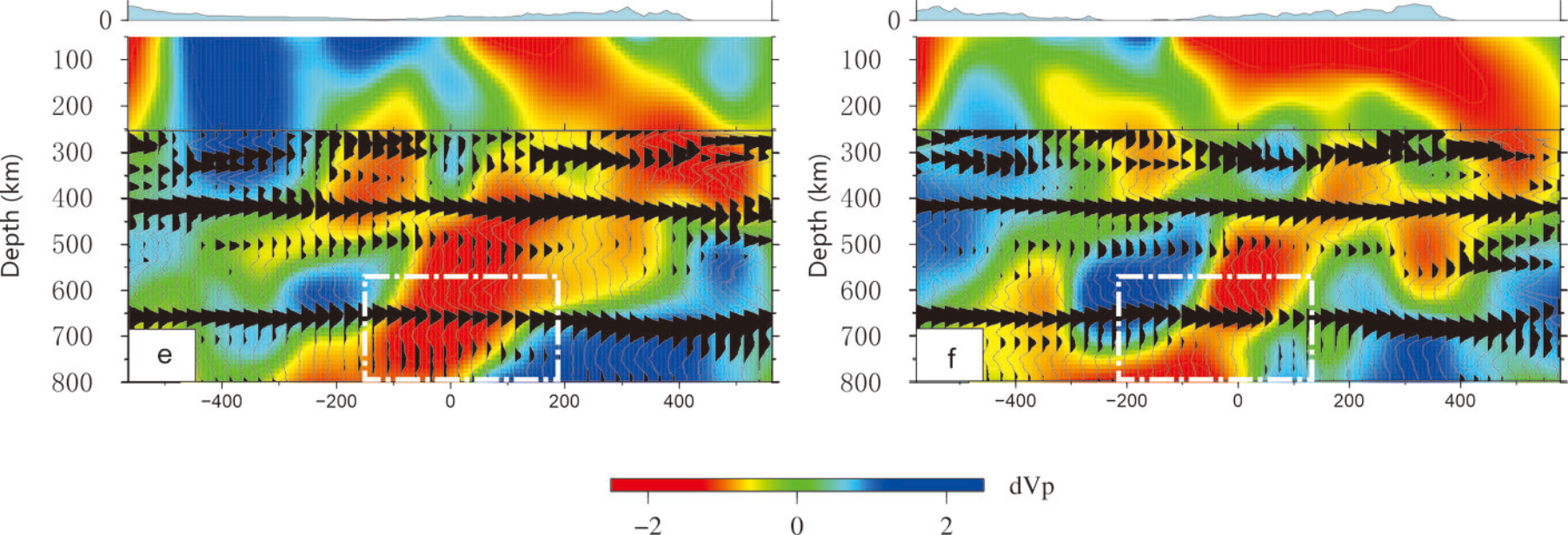
0
100
200
300
400
500
600
700
800
Depth (km)
e
f
−400
−200
0
200
400
dVp
−2
0
2

Figure 4.

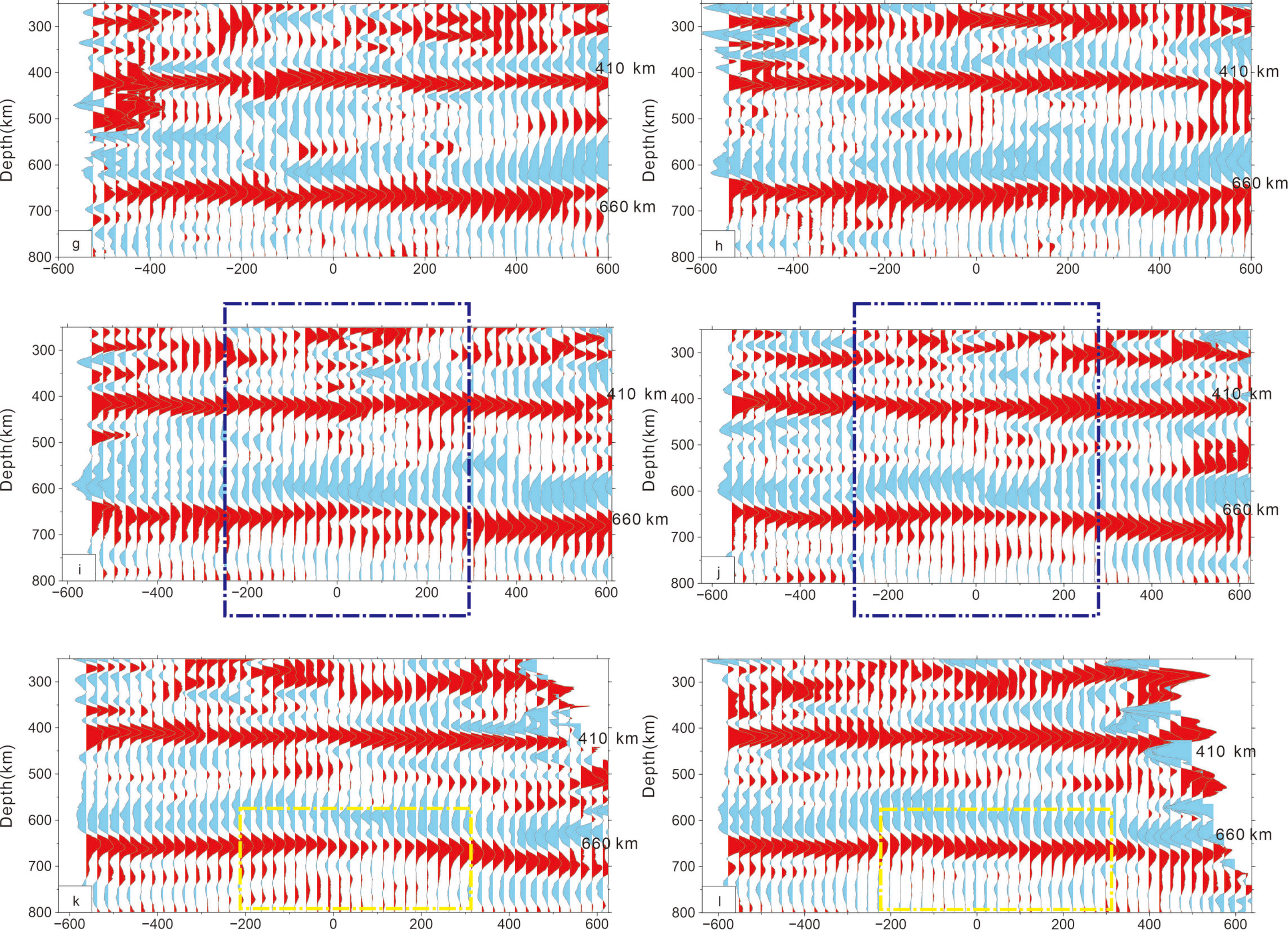
Depth(km)
300
400
500
600
700
800
−600
−400
−200
0
200
400
600
410 km
660 km
g
h
i
j
k
l

Figure 5.

a

b

c

d

e

f

g

Songliao Basin

WDL

CBS

116°

120°

124°

128°

132°

48°

44°

40°

(km)

−5000

0

5000

Count

200

400

600

800

420

660

690

240

260

Figure 6.

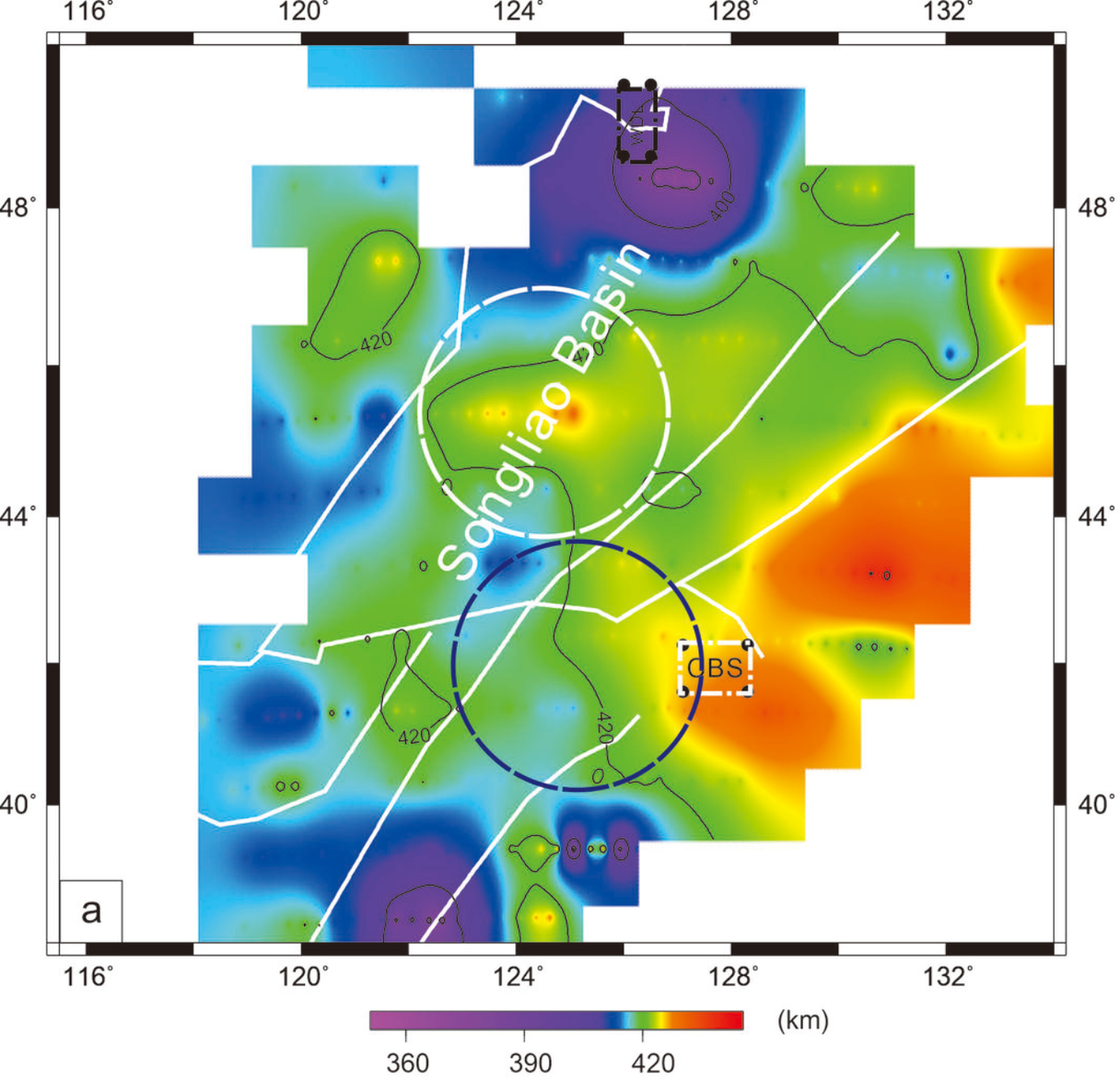
116°
120°
124°
128°
132°
48°
44°
40°
WDL
CBS
Songliao Basin
400
420
420
420
a
360
390
420
(km)

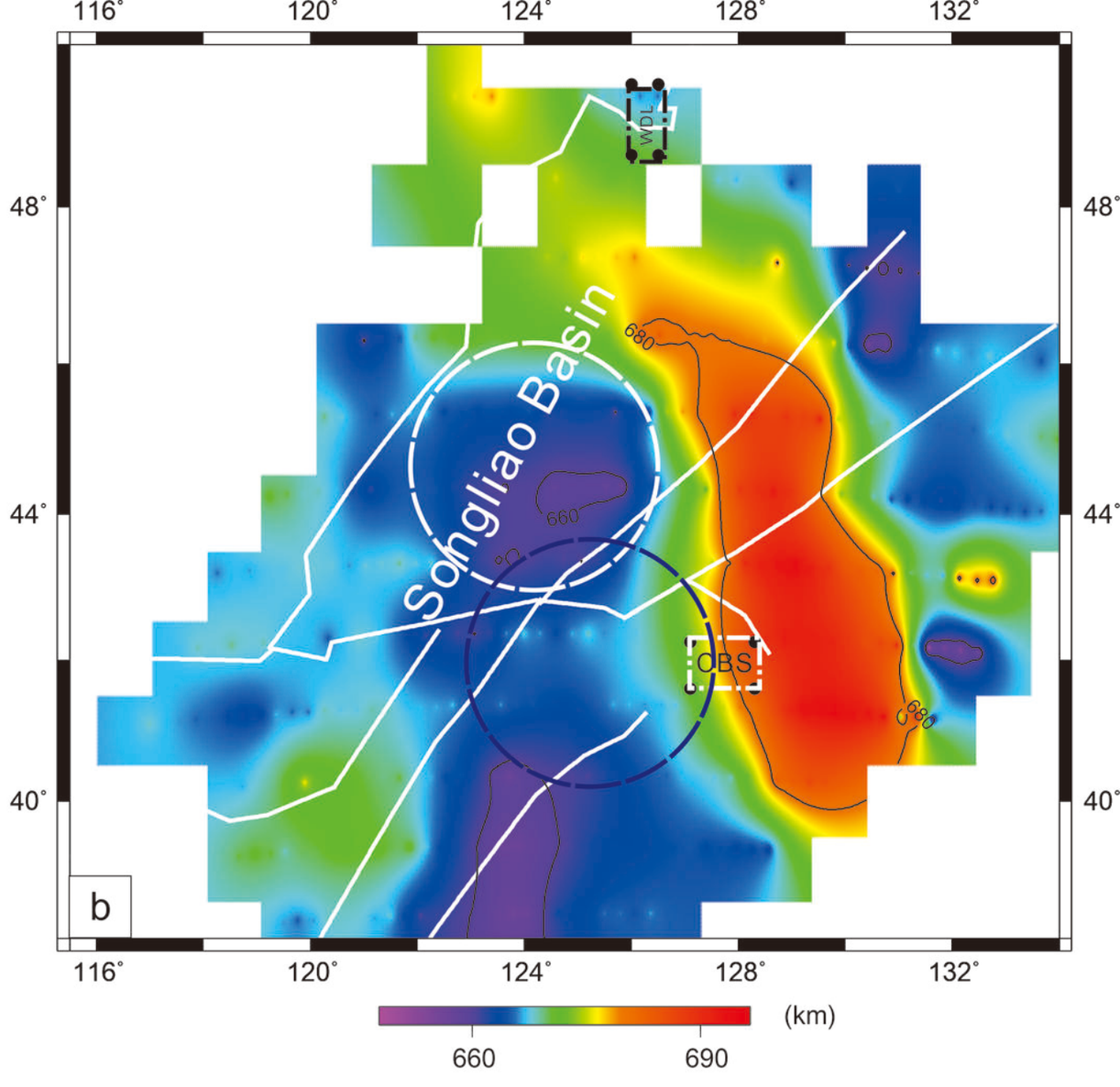
116°
120°
124°
128°
132°
48°
44°
40°
WDL
CBS
Songliao Basin
660
680
680
b
660
690
(km)

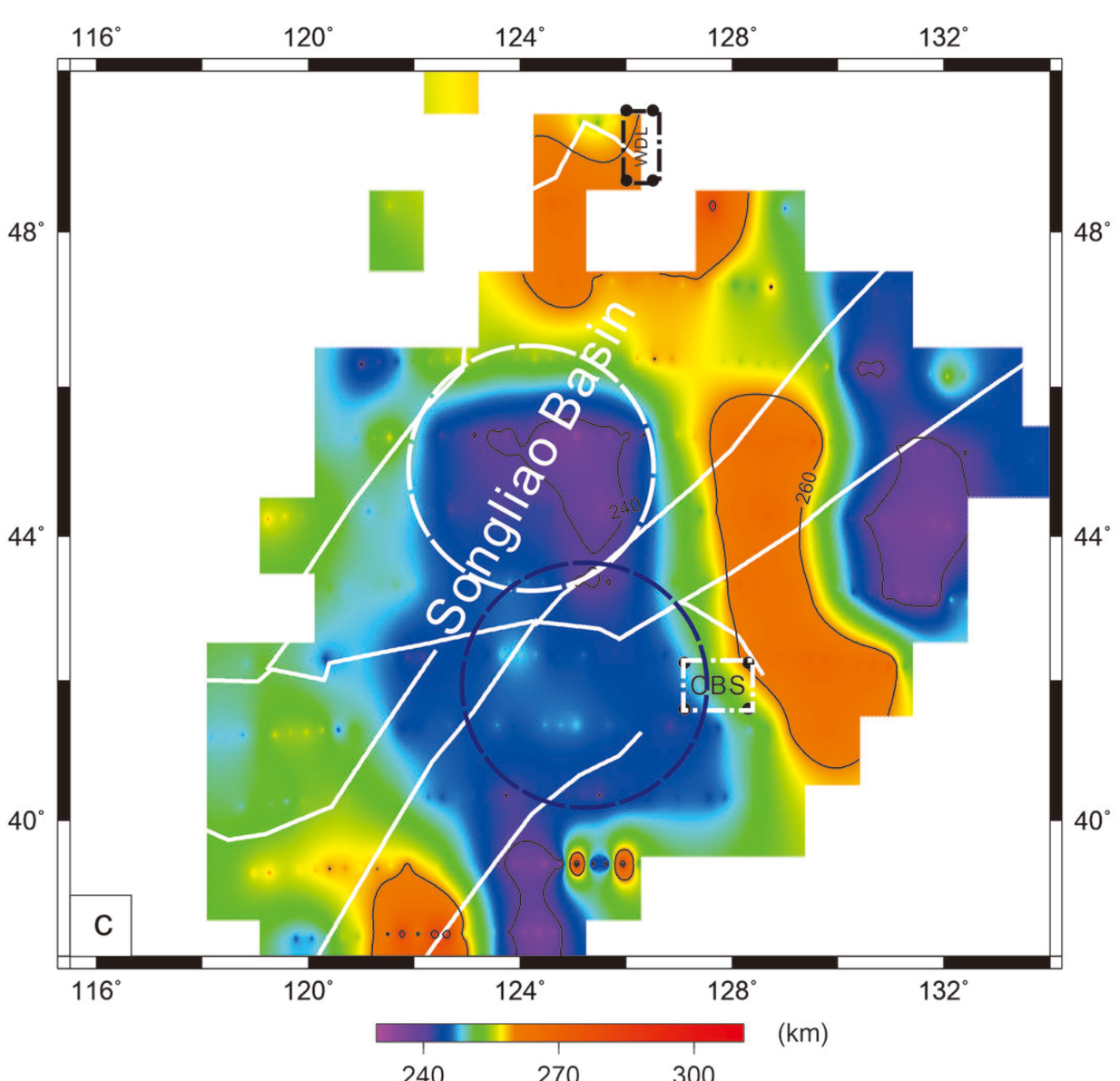
116°
120°
124°
128°
132°
48°
44°
40°
WDL
CBS
Songliao Basin
240
260
c
240
270
300
(km)

Figure 7.

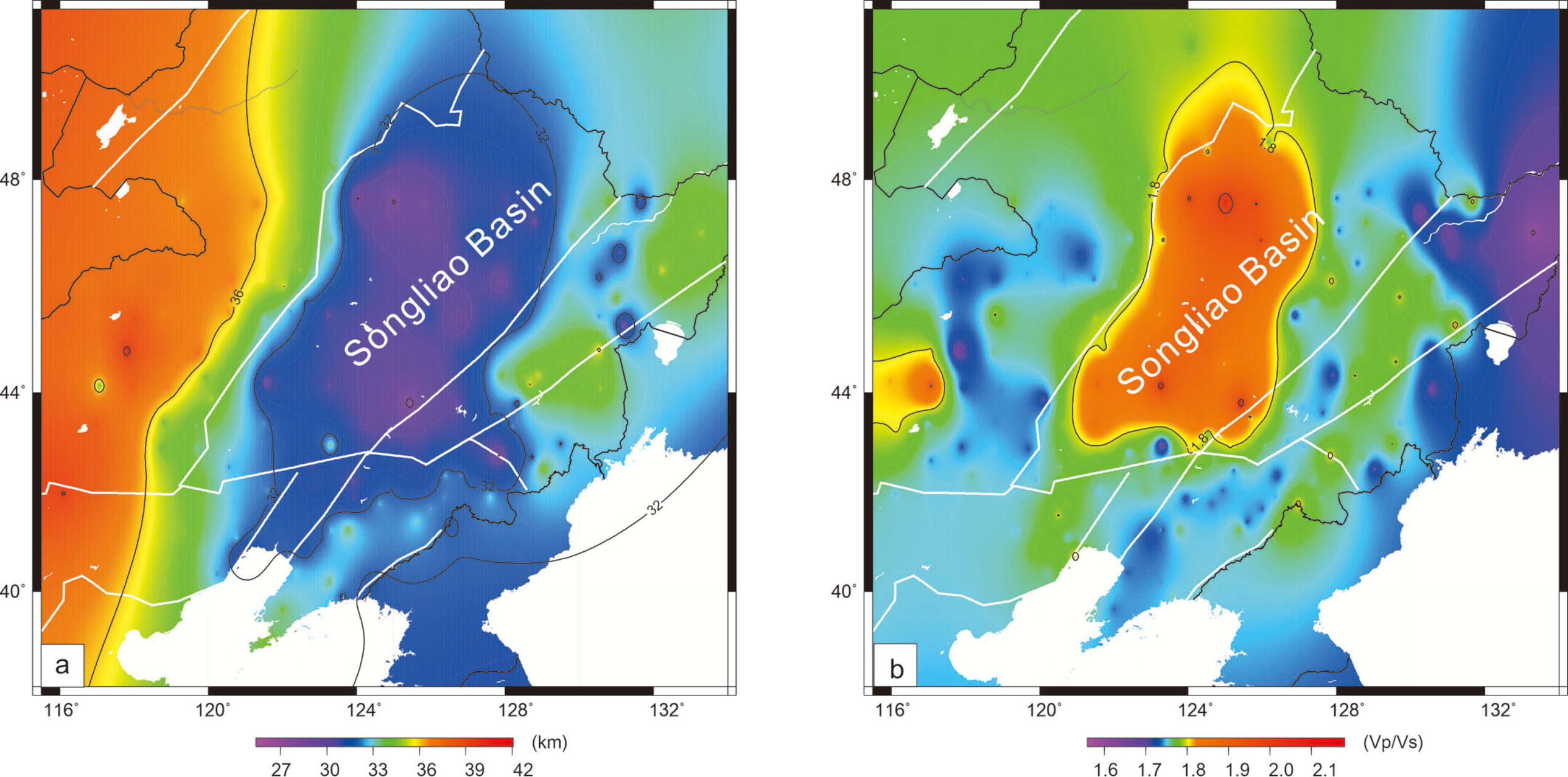
Songliao Basin
32
36
48°
44°
40°
116°
120°
124°
128°
132°
a
(km)
27
30
33
36
39
42
Songliao Basin
1.8
1.87
0
b
(Vp/Vs)
1.6
1.7
1.8
1.9
2.0
2.1

Figure 8.

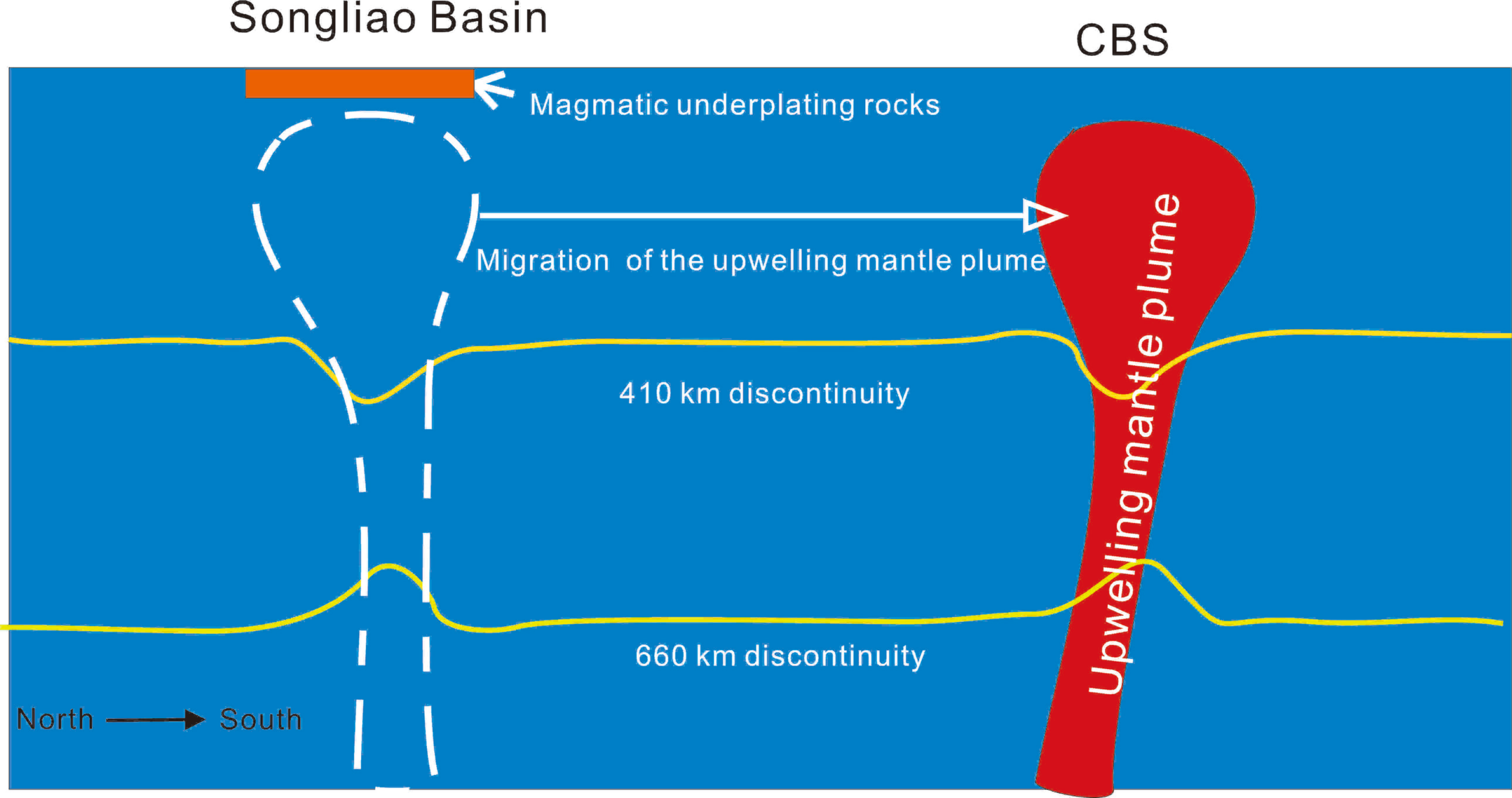
Songliao Basin
CBS
Magmatic underplating rocks
Migration of the upwelling mantle plume
410 km discontinuity
660 km discontinuity
Upwelling mantle plume
North
South